

# U-Net-Based Generative Joint Source-Channel Coding for Wireless Image Transmission

Ming Ye, *Member, IEEE*, Kui Cai, *Senior Member, IEEE*, Cunhua Pan, *Senior Member, IEEE*, Zhen Mei, *Member, IEEE*, Wanting Yang, and Chunguo Li, *Senior Member, IEEE*

**Abstract**—Deep learning (DL)-based joint source-channel coding (JSCC) methods have achieved remarkable success in wireless image transmission. However, these methods either focus on conventional distortion metrics that do not necessarily yield high perceptual quality or incur high computational complexity. In this paper, we propose two DL-based JSCC (DeepJSCC) methods that leverage deep generative architectures for wireless image transmission. Specifically, we propose G-UNet-JSCC, a scheme comprising an encoder and a U-Net-based generator serving as the decoder. Its skip connections enable multi-scale feature fusion to improve both pixel-level fidelity and perceptual quality of reconstructed images by integrating low- and high-level features. To further enhance pixel-level fidelity, the encoder and the U-Net-based decoder are jointly optimized using a weighted sum of structural similarity and mean-squared error (MSE) losses. Building upon G-UNet-JSCC, we further develop a DeepJSCC method called cGAN-JSCC, where the decoder is enhanced through adversarial training. In this scheme, we retain the encoder of G-UNet-JSCC and adversarially train the decoder’s generator against a patch-based discriminator. cGAN-JSCC employs a two-stage training procedure. The outer stage trains the encoder and the decoder end-to-end using an MSE loss, while the inner stage adversarially trains the decoder’s generator and the discriminator by minimizing a joint loss combining adversarial and distortion losses. Simulation results demonstrate that the proposed methods achieve superior pixel-level fidelity and perceptual quality on both high- and low-resolution images. For low-resolution images, cGAN-JSCC achieves better reconstruction performance and greater robustness to channel variations than G-UNet-JSCC.

**Index Terms**—Joint source-channel coding, deep learning, deep generative architectures, wireless image transmission.

## I. INTRODUCTION

THE proliferation of wireless multimedia applications, such as virtual reality and augmented reality, has imposed stringent low-latency and high-efficiency requirements on image/video transmission. To achieve reliable data transfer, wireless communication systems are carefully designed and optimized. In conventional communication systems following Shannon’s separation theorem [1], the transmitter comprises separate source and channel encoders. The source encoder compresses data by removing redundancy, whereas the channel

encoder introduces controlled redundancy to protect against channel impairments. At the receiver, a corresponding pair of channel and source decoders perform the inverse operations to reconstruct the original data.

Shannon established that the separation of source and channel coding is theoretically optimal in the asymptotic regime of infinite blocklength. However, the separation-based approach becomes highly suboptimal under the practical finite blocklength regime, especially for communication systems operating with strict latency and bandwidth constraints [2], [3]. Specifically, the substantial time required for compressing and decompressing high-rate image/video sources has become a primary bottleneck in end-to-end latency. Consequently, joint source-channel coding (JSCC), which unifies source and channel coding within a single architecture, is positioned as a viable solution for mission-critical 6G applications that require ultra-low latency, including autonomous vehicles and remote surgery [4]. Despite the established benefits of JSCC, designing effective JSCC approaches remains a long-standing challenge. Most research on traditional JSCC is confined to theoretical scenarios [5], [6] or focuses on jointly optimizing parameters of separately designed source and channel coding [7]–[9]. This limitation stems both from a scarcity of practical JSCC methods and from the lack of theoretical performance bounds on the achievable mean squared-error (MSE) distortion for lossy JSCC at finite blocklengths [10], particularly for practical sources like images.

Recently, the introduction of deep neural networks (DNNs) has rapidly advanced deep learning (DL)-based JSCC (DeepJSCC) methods. These DNN-based schemes establish an end-to-end learning framework, enabling a direct mapping from source signals to continuous channel inputs at the encoder and the inverse mapping at the decoder. This is achieved through the powerful ability of DNNs to extract inherent features and implicitly learn to compensate for channel impairments [11]–[13]. For example, the DeepJSCC method proposed in [14] is a seminal work for wireless image transmission, as it is the first to operate without explicit compression or error correction codes. It demonstrates superior performance over traditional separation-based systems that combine a source codec (e.g., JPEG) with a channel code such as low-density parity-check (LDPC) codes. The initial DeepJSCC framework was subsequently extended to handle multi-path fading channels [15], as well as to incorporate adaptive bandwidth [16], [17] and rate control [18], [19] for wireless image transmission. Following these developments, the authors of [20], [21] extended the DeepJSCC approach to multiple-

M. Ye, K. Cai, and W. Yang are with the Singapore University of Technology and Design, Singapore 487372 (e-mail: 230198460@aa.seu.edu.cn; cai\_kui@sutd.edu.sg; wanting\_yang@sutd.edu.sg).

C. Pan and C. Li are with the National Mobile Communications Research Laboratory, Southeast University, Nanjing 210096, China (e-mail: cpan@seu.edu.cn; chunguoli@seu.edu.cn).

Z. Mei is with the School of Electronic and Optical Engineering, Nanjing University of Science and Technology, Nanjing 210094, China (e-mail: meizhen@njust.edu.cn).

input multiple-output (MIMO) systems by exploiting the self-attention mechanism of the Vision Transformer. Research on DeepJSCC approaches has also expanded to include its security in semantic communication systems, employing both conventional encryption methods [22] and encryption schemes based on neural networks [23], [24]. Although training DeepJSCC schemes is computationally intensive, their deployment is highly efficient. This is because the complexity of both encoding and decoding during inference is significantly lower than that of traditional systems that execute advanced image codecs followed by capacity-approaching channel codecs. However, a vast majority of the aforementioned DeepJSCC approaches do not focus on the perceptual semantic quality between the source and reconstructed images. Instead, they rely primarily on metrics such as peak signal-to-noise ratio (PSNR) or structural similarity index measure (SSIM), which serve as both the end-to-end measure of distortion and the training loss function.

Inspired by the success of deep generative models (DGMs) in image generation [25]–[27], researchers have proposed DeepJSCC methods based on DGMs for wireless image transmission. These methods leverage DGMs such as diffusion models [28], variational autoencoders (VAEs) [29], [30], and generative adversarial networks (GANs) [31], [32]. Specifically, a three-stage DeepJSCC approach based on diffusion models was proposed in [28] for wireless image transmission in semantic communication systems. The authors of [29] proposed a VAE-based DeepJSCC scheme for distributed Gaussian sources over a multiple-access additive white Gaussian noise (AWGN) channel, exploiting a key regularization mechanism to enhance reconstruction quality. In [30], a DeepJSCC method was proposed for analog noise channels by using the VAE loss function to characterize the rate-distortion trade-off. Its efficacy was demonstrated through simulations involving Gaussian sources over AWGN channels. By adversarially training a legitimate autoencoder against an adversary network, the DeepJSCC method proposed in [31] achieved a privacy-distortion trade-off for secure image transmission over a noisy wiretap channel. A DeepJSCC scheme was proposed in [32] to enhance the reconstruction quality of images over multipath fading channels by adversarially training a decoder network with a discriminator. However, these DeepJSCC methods [28]–[32] rely solely on conventional pixel-wise distortion metrics and fail to incorporate the learned perceptual image patch similarity (LPIPS) metric [33] that better aligns with human perception. Furthermore, the generator architecture in [32] constrains perceptual quality, as it lacks efficient structures such as the StyleGAN-2 generator employed in [34], thereby limiting its capacity for high-quality image reconstruction. Additionally, the method fails to clearly explain how the adversarially trained decoder is jointly optimized with the encoder. The authors of [35] proposed the first DeepJSCC scheme that leverages a pre-trained StyleGAN-2 generator to improve both pixel-level fidelity and perceptual quality of reconstructed images for wireless image transmission. However, this approach is not only confined to face images but also incurs high computational complexity, as both its encoder and decoder employ complex modules like attention mechanisms

and residual blocks.

In our prior works [36]–[38], GAN variants leveraging a generator based on the U-Net architecture in [27], [39] have been successfully applied to channel estimation by formulating it as an image-to-image translation task. Inspired by this success, we propose two DeepJSCC methods for wireless image transmission. These methods are based on deep generative architectures, specifically a conditional GAN (cGAN) framework with U-Net-based generators. In particular, we propose G-UNet-JSCC, which comprises an encoder and a U-Net-based generator serving as the decoder. In the U-Net-based decoder, the skip connections enable multi-scale information fusion by combining low-level features (e.g., textures and edges) with high-level features (e.g., overall structure). This fusion improves both the pixel-level fidelity (e.g., PSNR and SSIM) and the perceptual quality (e.g., LPIPS), particularly under low signal-to-noise ratio (SNR) conditions. This design achieves a favorable trade-off between complexity and performance. Compared to prior DeepJSCC schemes that employ almost symmetric encoder-decoder structures (e.g., [14], [32]) or complex encoders (e.g., [20], [35]), our G-UNet-JSCC adopts an asymmetric design: a relatively simple encoder paired with a powerful U-Net decoder. To further improve the pixel-level fidelity, we train the encoder and the decoder end-to-end by minimizing a weighted sum of MSE and SSIM losses. Building upon G-UNet-JSCC, we then propose a DeepJSCC method, named cGAN-JSCC, which enhances the decoder of G-UNet-JSCC via adversarial training. In cGAN-JSCC, we retain the G-UNet-JSCC encoder and adversarially train the decoder’s U-Net-based generator against a patch-based discriminator. cGAN-JSCC employs a two-stage training procedure. In the outer stage, the encoder and the decoder are trained end-to-end using an MSE loss. In the inner stage, the generator and the discriminator are adversarially trained by minimizing a joint loss that combines adversarial and L1 losses [27]. This two-stage training strategy maintains high reconstruction performance through optimization in the outer stage and enhances robustness to channel variations via adversarial training in the inner stage. Extensive numerical experiments demonstrate that both the proposed methods achieve high reconstruction quality on high- and low-resolution images. For low-resolution images, cGAN-JSCC outperforms G-UNet-JSCC in terms of reconstruction performance and robustness.

The main contributions of this work can be summarized as follows:

- We employ a U-Net-based generator as the decoder in our JSCC frameworks. Its skip connections facilitate multi-scale feature fusion, integrating low-level details with high-level semantics. This design improves reconstruction quality and robustness under varying channel conditions, while maintaining a favorable trade-off between computational complexity and reconstruction quality. To our knowledge, this is the first work to develop JSCC methods employing U-Net-based generators for wireless image transmission, achieving both high pixel-level fidelity and perceptual quality.
- We first propose G-UNet-JSCC, a DeepJSCC scheme for wireless image transmission. Unlike existing DL-based

encoder-decoder structures, G-UNet-JSCC adopts an asymmetric architecture, pairing a simple encoder with a powerful U-Net-based decoder. This scheme improves both the pixel-level fidelity and the perceptual quality, especially in low SNR regimes. To further enhance the pixel-level fidelity, the encoder and the decoder are jointly optimized to minimize a weighted sum of the MSE and SSIM losses.

- We then propose cGAN-JSCC, which incorporates adversarial training into the JSCC decoder. In cGAN-JSCC, we keep the same encoder as G-UNet-JSCC and adversarially train the U-Net-based generator against a patch-based discriminator within the decoder. The cGAN-JSCC training follows a two-stage procedure: an outer stage for end-to-end optimization of the encoder and the decoder, and an inner stage within the decoder for adversarial training of the generator and the discriminator. This strategy maintains high reconstruction performance via the outer-stage optimization and improves robustness to channel variations through the inner-stage adversarial training.

- Extensive numerical experiments on multiple datasets demonstrate the superiority of cGAN-JSCC and G-UNet-JSCC in terms of pixel-level fidelity and perceptual quality on both low- and high-resolution images. Moreover, for low-resolution images, cGAN-JSCC exhibits superior performance and greater robustness to channel SNR variations compared to G-UNet-JSCC.

## II. SYSTEM MODEL

We consider a communication system in which a source signal is transmitted from a transmitter to a receiver over a noisy wireless channel. As shown in Fig. 1, the joint source-channel encoder in the G-UNet-JSCC method directly maps a real-valued source input (image)  $\mathbf{x} \in \mathbb{R}^n$  into a complex-valued channel input symbol vector  $\mathbf{z} \in \mathbb{C}^k$  for channel transmission. The encoded source image can be expressed as

$$\mathbf{z} = f_{\theta}(\mathbf{x}) \in \mathbb{C}^k, \quad (1)$$

where  $f_{\theta} : \mathbb{R}^n \rightarrow \mathbb{C}^k$  denotes the parameterized encoding function with parameters  $\theta$ . Here,  $n$  and  $k$  represent the source dimension and the channel dimension, respectively. The bandwidth compression ratio (BCR) is defined as  $r = k/n$ . A smaller  $r$  corresponds to a higher level of compression.

The output of the final convolutional layer of the encoder is transformed into a vector of complex-valued symbols. This vector, denoted as  $\tilde{\mathbf{z}}$ , is then normalized before being transmitted through the noisy wireless channel. To comply with the average transmit power constraint  $\bar{P}$ , the power normalization is performed according to:

$$\mathbf{z} = \sqrt{k\bar{P}} \frac{\tilde{\mathbf{z}}}{\sqrt{\tilde{\mathbf{z}}^H \tilde{\mathbf{z}}}}, \quad (2)$$

where  $\mathbf{z}$  is the normalized feature vector for transmission.

The normalized feature vector  $\mathbf{z}$  is corrupted by the wireless noisy channel, resulting in a corrupted signal  $\hat{\mathbf{z}}$ . This process can be modeled by a random corruption function  $\delta : \mathbb{C}^k \rightarrow \mathbb{C}^k$ . Specifically, the transfer function of the AWGN channel is given by

$$\hat{\mathbf{z}} = \delta(\mathbf{z}, \sigma^2) = \mathbf{z} + \mathbf{n}, \quad (3)$$

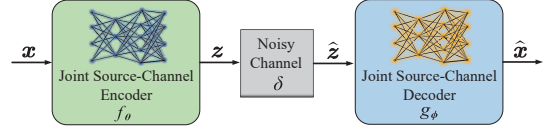


Fig. 1. Block diagram of the image transmission system for the proposed G-UNet-JSCC method.

where  $\mathbf{n}$  is AWGN following the distribution  $\mathbf{n} \sim \mathcal{CN}(\mathbf{0}, \sigma^2 \mathbf{I})$ , where  $\sigma^2$  denotes the average noise power.

The corrupted complex-valued channel output symbol vector  $\hat{\mathbf{z}}$  is then mapped into the reconstructed image  $\hat{\mathbf{x}}$  by the joint source-channel decoder using a decoding function  $g_{\phi} : \mathbb{C}^k \rightarrow \mathbb{R}^n$ , which is parameterized by the set of parameters  $\phi$ . The reconstructed image  $\hat{\mathbf{x}}$  can be expressed as

$$\hat{\mathbf{x}} = g_{\phi}(\hat{\mathbf{z}}) \in \mathbb{R}^n. \quad (4)$$

The objective of the entire pipeline is to jointly optimize the encoder and decoder parameters  $\theta$  and  $\phi$  to minimize the average distortion between the source image  $\mathbf{x}$  and its reconstruction  $\hat{\mathbf{x}}$ :

$$(\theta^*, \phi^*) = \arg \min_{\theta, \phi} \mathbb{E}_{p(\mathbf{x}, \hat{\mathbf{x}})} [d(\mathbf{x}, \hat{\mathbf{x}})], \quad (5)$$

where  $p(\mathbf{x}, \hat{\mathbf{x}})$  denotes the induced joint probability distribution of  $\mathbf{x}$  and  $\hat{\mathbf{x}}$ , and  $d(\mathbf{x}, \hat{\mathbf{x}})$  is an arbitrary distortion measure. Conventional metrics such as PSNR and SSIM do not adequately capture perceptual quality. Therefore, the objective of this work is to enhance both the pixel-wise fidelity and the perceptual quality of the reconstructions, particularly under low SNR conditions.

## III. PROPOSED METHODS

In this section, we propose two DeepJSCC methods based on deep generative architectures to improve both the pixel-level fidelity and the perceptual quality of reconstructed images for wireless image transmission. We first propose G-UNet-JSCC, a DeepJSCC method that comprises an encoder and a U-Net-based generator serving as the decoder. The skip connections in the U-Net-based decoder facilitate multi-scale feature fusion by combining low-level features with high-level features, thereby improving both the pixel-level fidelity and the perceptual quality. To further improve the pixel-level fidelity of reconstructed images, the encoder and the U-Net-based decoder are optimized jointly to minimize a weighted sum of MSE and SSIM losses. Furthermore, we propose cGAN-JSCC, an adversarially trained variant of G-UNet-JSCC. In cGAN-JSCC, we keep the same encoder as G-UNet-JSCC and adversarially train the generator against a patch-based discriminator within the decoder. The cGAN-JSCC method is trained through a two-stage procedure. The encoder and the U-Net-based generator are jointly optimized using an MSE loss in the outer training stage, while the U-Net-based generator and the discriminator are trained with a combination of adversarial and L1 losses in the inner training stage.

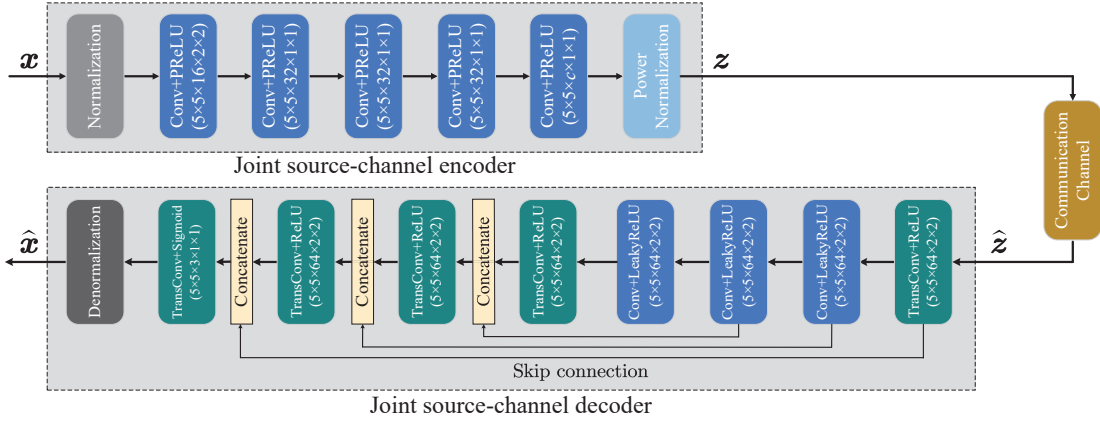


Fig. 2. Encoder and decoder DNN architectures of the proposed G-UNet-JSCC method.

### A. G-UNet-JSCC Framework

To enhance both the pixel-wise accuracy and the perceptual quality of reconstructed images, we propose a DeepJSCC framework, termed G-UNet-JSCC. The G-UNet-JSCC method consists of a deep encoder and a U-Net-based generator serving as the decoder. This end-to-end scheme jointly optimizes the encoding and decoding functions, which are parameterized by DNNs with learnable parameters  $\theta$  and  $\phi$ , respectively.

As illustrated in Fig. 2, the source image  $x$  is processed by the encoder in the G-UNet-JSCC method and normalized according to Eq. (2) at the final layer of the encoder to comply with the power constraint. Subsequently, the encoded signal  $z$  is transmitted over the wireless noisy channel characterized by the transfer function defined in Eq. (3). At the receiver, the corrupted signal  $\hat{z}$  is decoded by the U-Net-based decoder to reconstruct the source image:

$$\hat{x} = g_{\phi}(\delta(f_{\theta}(x), \sigma^2)). \quad (6)$$

The encoder and the decoder in the G-UNet-JSCC scheme are optimized end-to-end by minimizing a combined loss function:

$$\mathcal{L}_C(\theta, \phi) = \lambda_M \mathcal{L}_{\text{MSE}}(x, \hat{x}) + \lambda_S \mathcal{L}_{\text{SSIM}}(x, \hat{x}), \quad (7)$$

where  $\mathcal{L}_{\text{MSE}}$  and  $\mathcal{L}_{\text{SSIM}}$  denote the MSE and SSIM loss functions, respectively, and  $\lambda_M$  and  $\lambda_S$  are the two hyperparameters that control the relative importance of the respective loss functions. The combined loss function can be seen as a weighted sum of the loss functions  $\mathcal{L}_{\text{MSE}}$  and  $\mathcal{L}_{\text{SSIM}}$ . The objective of training the G-UNet-JSCC model is to find the optimal parameters  $(\theta^*, \phi^*)$  that minimize the combined loss:  $(\theta^*, \phi^*) = \arg \min_{\theta, \phi} \mathbb{E}[\mathcal{L}_C(\theta, \phi)]$ .

To achieve a better trade-off between computational complexity and reconstruction quality, we employ a DNN architecture comprising an encoder and a U-Net-based decoder, as depicted in Fig. 2. The U-Net-based decoder, with its efficient skip connections, is particularly effective for image reconstruction tasks. As a concrete example to illustrate the architecture of G-UNet-JSCC, we use images of dimensions  $256 \times 256 \times 3$  (i.e., height, width, and color channels) cropped from the Celeb-HQ dataset [35], [40]. At the encoder, the

source image  $x$  is first processed by a normalization layer. The normalization layer scales the input pixel values of the source image from  $[0, 255]$  to  $[0, 1]$  through division by the maximum pixel value 255 for 8-bit images, which helps mitigate potential gradient explosion. The normalized image is then processed by five convolutional layers. The first convolutional layer performs downsampling to extract low-level features. The subsequent four convolutional layers, all operating at a fixed resolution, conduct non-linear transformations to synthesize features, with the final convolutional layer producing  $c$  feature maps of dimensions  $128 \times 128$ . All convolutional layers in the encoder use the parametric rectified linear unit (PReLU) as their activation functions. To satisfy the power constraint, the final convolutional layer at the encoder, which comprises  $c$  output channels, is followed by a power normalization layer. The number of output channels  $c$  can be adjusted to control the BCR. Note that the real-valued output from the encoder's final convolutional layer is transformed into a vector of  $k$  complex-valued channel input symbols before the power normalization layer. This power normalization layer, as defined in Eq. (2), produces the normalized feature vector  $z$  for transmission. The specific configurations of these hyperparameters used in our experiments are provided in Fig. 2. In Fig. 2, the notation  $F \times F \times K \times S_h \times S_w$  defines a (transposed) convolutional layer, where  $K$  denotes the number of filters with a spatial size of  $F \times F$ , and  $S_h \times S_w$  represents the stride in the height and width dimensions, respectively.

The corrupted signal  $\hat{z}$ , a vector of  $k$  complex-valued channel output symbols, is converted into a vector of  $2k$  real-valued symbols by concatenating its real and imaginary components. The real-valued vector is then reshaped into a real-valued channel output of dimensions  $128 \times 128 \times c$ , which serves as the input of the U-Net-based decoder. After that, the channel output is first upsampled by a transposed convolutional layer, yielding 64 feature maps of dimensions  $256 \times 256$ . Subsequently, these feature maps are processed and downsampled by three convolutional layers to generate 64 feature maps of dimensions  $32 \times 32$ . Following this, the resulting feature maps are progressively upsampled by the next three transposed convolutional layers to produce 64 feature

---

**Algorithm 1** G-UNet-JSCC Joint Training Algorithm
 

---

```

1: Input: Training dataset  $\mathcal{D} = \{\mathbf{x}_i\}_{i=1}^T$ , the number of
   epochs  $E$ , BCR set  $R$ , batch size  $B$ , SNR set  $S$ , learning
   rate  $\eta$ 
2: Output: Trained encoders  $f_\theta$  and decoders  $g_\phi$  for all
    $(r, \gamma)$  combinations
3: for each bandwidth ratio  $r \in R$  do
4:   for each SNR value  $\gamma \in S$  do
5:     Initialize encoder  $f_\theta$  and decoder  $g_\phi$ 
6:     Compute noise variance:  $\sigma^2 \leftarrow 10^{-\gamma/10}$ 
7:     for epoch = 1 to  $E$  do
8:       Forward pass through JSCC pipeline
9:       Sample a minibatch of size  $B$  from  $\mathcal{D}$ 
10:      Encode the source image  $\mathbf{x}$  to the complex-
        valued symbol vector  $\mathbf{z}$  using Eq. (1):  $\mathbf{z} \leftarrow f_\theta(\mathbf{x})$ 
11:      Add the AWGN to the vector  $\mathbf{z}$  using Eq. (3)
        and obtain the corrupted signal  $\hat{\mathbf{z}}$ 
12:      Decode to reconstruct the image  $\hat{\mathbf{x}}$  from the
        corrupted signal  $\hat{\mathbf{z}}$ :  $\hat{\mathbf{x}} \leftarrow g_\phi(\hat{\mathbf{z}})$ 
13:      Compute joint reconstruction loss
14:      Compute reconstruction loss  $\mathcal{L}_C$  using Eq. (7)
15:      Joint parameter update via backpropagation
16:      Update parameters  $\{\theta, \phi\}$  by gradient descent
        on  $\mathcal{L}_C$ :  $\theta, \phi \leftarrow \theta, \phi - \eta \nabla_{\theta, \phi} \mathcal{L}_C$ 
17:    end for
18:    Save trained models for current  $(r, \gamma)$  configura-
        tion: encoder  $f_\theta$  and decoder  $g_\phi$ 
19:  end for
20: end for

```

---

maps of size  $256 \times 256$ . Then, the last transposed convolutional layer reduces the channel dimension from 64 to 3, producing a  $256 \times 256 \times 3$  tensor. Finally, a denormalization layer is applied to scale the pixel values from the output of the decoder’s final transposed convolutional layer to the  $[0, 255]$  range, yielding the final reconstructed image  $\hat{\mathbf{x}}$  of size  $256 \times 256 \times 3$ . In the decoder, the transposed convolutional layers use the rectified linear unit (ReLU) activation function, except for the final transposed convolutional layer, which employs the Sigmoid activation function. The convolutional layers in the decoder use the leaky ReLU (LeakyReLU) activation function.

The U-Net-based decoder incorporates its own downsampling-upsampling path to facilitate multi-scale feature fusion via internal skip connections. These connections integrate the upsampled feature maps with the feature maps from other parts of the decoder at the corresponding scale. For example, as shown in Fig. 2, the  $256 \times 256$  feature maps from the decoder’s fourth transposed convolutional layer are combined with those from the decoder’s first transposed convolutional layer via skip connections. Similarly, the  $64 \times 64$  feature maps from the second transposed convolutional layer are fused with those from the decoder’s second convolutional layer. Despite being corrupted by channel noise, the output from the encoder that serves as the input to the U-Net-based decoder retains rich low-level information such as textures and edges. This information provides a foundational skeleton

for the decoder to reconstruct the source image, preventing it from hallucinating content and thereby ensuring pixel-wise consistency. The skip connections supply corrupted low-level information, while the backbone path provides corrupted high-level information. Although both the low-level and high-level information are noisy, their noise patterns are correlated and their content is complementary. Without these skip connections, the decoder is prone to generating structurally distorted images. Moreover, by leveraging both the detailed guidance from skip connections and the image priors learned from training data, the U-Net-based decoder effectively restores and enhances noise-corrupted regions without relying on complex modules like attention mechanisms. This results in clearer and more natural textures and improves the decoder’s robustness to channel variations, which is crucial for enhancing perceptual quality.

The training procedure of the G-UNet-JSCC scheme is illustrated in Algorithm 1. Although the encoder and the U-Net-based decoder are end-to-end trained, they can be deployed separately after training. Compared to existing DL-based encoder-decoder structures such as almost symmetric structures or complex encoder structures, our G-UNet-JSCC adopts a deliberately asymmetric architecture. It pairs a relatively simple encoder with a powerful U-Net-based decoder. Hence, the G-UNet-JSCC scheme is particularly suitable for practical scenarios where the encoder is resource-constrained (e.g., on mobile devices), while the decoder can leverage more computational resources at the receiver. To maximize perceptual quality and minimize distortion, our G-UNet-JSCC employs a U-Net-based generator as its decoder. This design is inspired by the success of deep generative architectures like cGANs, which often use U-Net structures in their generators for high-fidelity image synthesis.

### B. cGAN-JSCC Framework

In the previous subsection, to enhance both the pixel-wise accuracy and the perceptual quality of reconstructed images, we propose G-UNet-JSCC, a DeepJSCC method comprising an encoder and a U-Net-based decoder. Building on this, we propose the cGAN-JSCC method, which is based on a cGAN framework inspired by the Pix2Pix architecture [27]. In this design, we keep the encoder unchanged from that of G-UNet-JSCC but adversarially train the decoder (i.e., the U-Net-based generator) against a patch-based discriminator. Unlike standard GANs for random generation, the cGAN-JSCC decoder takes the noisy and distorted channel output from the encoder as its conditional input and learns to produce more accurate reconstructions via adversarial training. cGAN-JSCC is designed to further improve the perceptual quality of reconstructions and enhance the decoder’s robustness to channel variations when dealing with low-resolution images. The cGAN-JSCC method employs a two-stage training procedure. In the outer training stage, the encoder and the decoder are trained end-to-end using an MSE loss. In the inner training stage, we keep the encoder fixed and fine-tune the decoder by introducing adversarial training. Specifically, the U-Net-based generator and the discriminator are jointly optimized using a composite loss that combines the adversarial loss and the L1 loss.

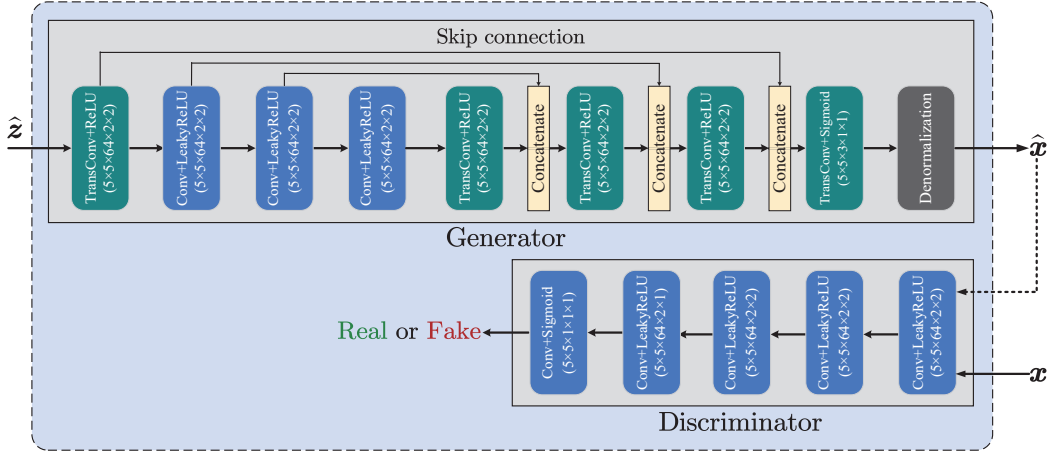


Fig. 3. Architecture of the adversarially trained decoder in cGAN-JSCC.

As shown in Fig. 3, the adversarially trained decoder in cGAN-JSCC takes the corrupted signal  $\hat{z}$  as its input. At the receiver, the signal is decoded by the decoder to reconstruct the source image. Therefore, the image reconstructed by the decoder can be expressed as

$$\hat{x} = g_\psi(\delta(f_\theta(x), \sigma^2)). \quad (8)$$

where  $g_\psi$  denotes the decoding function parameterized by  $\psi$  for cGAN-JSCC. Subsequently, both the reconstructed image  $\hat{x}$  and the original image  $x$  are fed into the discriminator. In the decoder, the U-Net-based generator and the discriminator are denoted as  $G$  and  $D$ , respectively. Thus, we also have  $\hat{x} = G(\hat{z})$ . During adversarial training, the U-Net-based generator learns to produce realistic image reconstructions that deceive the discriminator, while the discriminator strives to distinguish between the original image and the reconstructed one.

Unlike a regular discriminator that outputs a scalar value, we adopt a patch-based discriminator architecture [36]–[38]. In this architecture, the discriminator maps the input to a matrix of responses, where each element corresponds to a distinct receptive field (or patch) and represents a local real/fake classification score. During training, our discriminator learns to classify each local patch of the input as either real (from  $x$ ) or fake (from  $G(\hat{z})$ ). Subsequently, the patch-based discriminator averages these local scores to produce a final decision on whether the input image is real or fake. This patch-level feedback mechanism enables the patch-based discriminator to guide the generator in improving its reconstructions more effectively than a regular discriminator. Our discriminator comprises five convolutional layers. The first four layers employ the LeakyReLU activation function, while the final layer uses the Sigmoid activation function to scale the output values to the range  $[0, 1]$ .

The discriminator outputs are denoted as  $D_{\text{real}} = D(x)$  for real images and  $D_{\text{fake}} = D(G(\hat{z}))$  for reconstructed images produced by the U-Net-based generator. Each element in  $D_{\text{real}}$  or  $D_{\text{fake}}$  represents the probability that the corresponding patch of the input is real. This matrix of probabilities ranging between 0 and 1 provides detailed feedback to the generator,

guiding it to produce more realistic image reconstructions. Specifically, each element in  $D_{\text{real}}$  corresponds to the probability assigned by the discriminator that a specific patch of  $x$  is real. Conversely, each element in  $D_{\text{fake}}$  indicates the probability assigned by the discriminator that the corresponding patch of  $G(\hat{z})$  is real (i.e., it successfully deceives the discriminator). During adversarial training, the patch-based discriminator learns to push each element of  $D_{\text{real}}$  close to 1, while the U-Net-based generator is trained to make each element in  $D_{\text{fake}}$  approach 1. Thus, within the proposed decoder, the U-Net-based generator and the patch-based discriminator are trained adversarially.

The core of the proposed cGAN-JSCC method lies in the adversarial training between the U-Net-based generator and the patch-based discriminator, which minimizes an adversarial loss. The minimization of this loss has been demonstrated to effectively capture both global semantics and local textures, producing visually appealing generated images [42], [43]. The adversarial loss, referred to as the GAN loss, can be formulated as

$$\mathcal{L}_{\text{GAN}}(D, G) = \mathbb{E}_x [\log D(x)] + \mathbb{E}_{\hat{z}} [\log (1 - D(G(\hat{z})))] . \quad (9)$$

During training, the discriminator  $D$  aims to maximize  $\mathcal{L}_{\text{GAN}}$  (by correctly classifying real and fake images), while the generator  $G$  aims to minimize it (by fooling  $D$ ). The loss function for training the generator can be expressed as

$$\mathcal{L}_G(D, G) = \mathbb{E}_{\hat{z}} [\log (1 - D(G(\hat{z})))] . \quad (10)$$

To further improve the quality of the reconstructed images and stabilize the training process, we incorporate an L1 loss  $\mathcal{L}_{L1}$  [27], [41] into the generator's loss function. The L1 loss is defined as:

$$\mathcal{L}_{L1}(G) = \lambda_1 \mathbb{E}_{\hat{z}, x} [\|\mathbf{x} - G(\hat{z})\|_1] , \quad (11)$$

where  $\lambda_1$  is the weighting coefficient for the term  $\mathbb{E}_{\hat{z}, x} [\|\mathbf{x} - G(\hat{z})\|_1]$ . Then, the loss defined in Eq. (10) for training the generator can be rewritten as

$$\mathcal{L}_{G2}(D, G) = \mathbb{E}_{\hat{z}} [\log (1 - D(G(\hat{z})))] + \lambda_1 \mathbb{E}_{\hat{z}, x} [\|\mathbf{x} - G(\hat{z})\|_1] . \quad (12)$$

---

**Algorithm 2** cGAN-JSCC Joint Training Algorithm
 

---

- 1: **Input:** Training dataset  $\mathcal{D} = \{\mathbf{x}_i\}_{i=1}^T$ , the number of epochs  $E$ , BCR set  $R$ , batch size  $B$ , SNR set  $S$ , learning rate  $\eta$
  - 2: **Output:** Trained encoders  $f_\theta$  and decoders  $g_\psi$  for all  $(r, \gamma)$  combinations
  - 3: **for** each bandwidth ratio  $r \in R$  **do**
  - 4:   **for** each SNR value  $\gamma \in S$  **do**
  - 5:     Initialize encoder  $f_\theta$  and decoder  $g_\psi$
  - 6:     Compute noise variance:  $\sigma^2 \leftarrow 10^{-\gamma/10}$
  - 7:     **for** epoch = 1 to  $E$  **do**
  - 8:       **Forward pass through JSCC pipeline**
  - 9:       Sample a minibatch of size  $B$  from  $\mathcal{D}$
  - 10:       Encode the source image  $\mathbf{x}$  to the complex-valued symbol vector  $\mathbf{z}$  using Eq. (1):  $\mathbf{z} \leftarrow f_\theta(\mathbf{x})$
  - 11:       Add the AWGN to the vector  $\mathbf{z}$  using Eq. (3) and obtain the corrupted signal  $\hat{\mathbf{z}}$
  - 12:       **GAN forward pass**
  - 13:       Feed  $\hat{\mathbf{z}}$  to the generator  $G$  to reconstruct the image:  $\hat{\mathbf{x}} \leftarrow G(\hat{\mathbf{z}})$
  - 14:       Compute discriminator outputs for real and reconstructed images:  $D_{\text{real}} \leftarrow D(\mathbf{x})$ ,  $D_{\text{fake}} \leftarrow D(\hat{\mathbf{x}})$
  - 15:       **Compute losses**
  - 16:       Compute the loss  $\mathcal{L}_{C2}$  according to Eq. (15)
  - 17:       Compute the generator loss  $\mathcal{L}_{G2}$  using Eq. (12)
  - 18:       Compute the discriminator loss  $\mathcal{L}_D$  according to Eq. (9)
  - 19:       **Joint parameter update via backpropagation**
  - 20:       Update parameters  $\{\theta, \psi\}$  by gradient descent on  $\mathcal{L}_{C2}$ :  $\theta, \psi \leftarrow \theta, \psi - \eta \nabla_{\theta, \psi} \mathcal{L}_{C2}$
  - 21:       Update generator parameters  $\varphi_G$  by descending the gradient of  $\mathcal{L}_{G2}$ :  $\varphi_G \leftarrow \varphi_G - \eta \nabla_{\varphi_G} \mathcal{L}_{G2}$
  - 22:       Update discriminator parameters  $\varphi_D$  by gradient descent on  $\mathcal{L}_D$ :  $\varphi_D \leftarrow \varphi_D - \eta \nabla_{\varphi_D} \mathcal{L}_D$
  - 23:       **end for**
  - 24:       Save trained models for current  $(r, \gamma)$  configuration: encoder  $f_\theta$  and decoder  $g_\psi$
  - 25:     **end for**
  - 26: **end for**
- 

Thus, the overall adversarial training objective for the decoder in cGAN-JSCC is given by the following minimax optimization problem:

$$\min_{\varphi_G} \max_{\varphi_D} [\mathcal{L}_{\text{GAN}}(D, G) + \mathcal{L}_{\text{L1}}(G)], \quad (13)$$

where  $\varphi_G$  and  $\varphi_D$  denote the parameter sets of the U-Net-based generator and the discriminator, respectively. The decoder parameters  $\psi$  consist of the generator parameters  $\varphi_G$  and the discriminator parameters  $\varphi_D$ .

The total loss can be expressed as  $\mathcal{L}_{\text{total}} = \mathcal{L}_{\text{GAN}}(D, G) + \mathcal{L}_{\text{L1}}(G)$ . To optimize this objective, the U-Net-based generator and the discriminator within the adversarially trained decoder are trained alternately to address the minimax problem. In each iteration, the parameters of one network are fixed while those of the other are updated. Specifically, during the generator's update phase, the discriminator parameters  $\varphi_D$  are fixed,

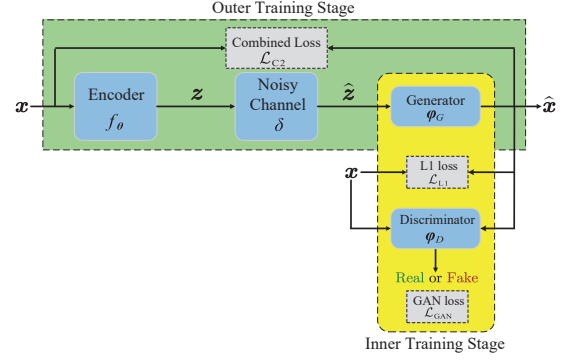


Fig. 4. Two-stage training procedure for the cGAN-JSCC scheme.

and the generator aims to minimize the total loss to fool the discriminator. During the discriminator's update phase,  $\varphi_G$  is fixed, and the discriminator aims to maximize the adversarial loss  $\mathcal{L}_{\text{GAN}}(D, G)$  to better distinguish the source images from the reconstructed ones. This adversarial training process enhances the cGAN-JSCC method's robustness to diverse channel conditions and drives the generator to produce more realistic and accurate reconstructed images, especially for low-resolution images. Consequently, the optimal generator  $G^*$  is obtained by solving the following minimax optimization problem:

$$G^* = \arg \min_G \max_D [\mathcal{L}_{\text{GAN}}(D, G) + \mathcal{L}_{\text{L1}}(G)]. \quad (14)$$

To prevent potential conflicts between the encoder's loss objective and the adversarial training within the decoder, we simplify the combined loss defined in Eq. (7) for the outer training stage. Specifically, we modify this combined loss by setting its weights to  $\lambda_M = 1$  and  $\lambda_S = 0$ . This reduces the combined loss to the MSE loss, ensuring that the encoder and decoder are optimized solely for reconstruction accuracy, without interference from adversarial or L1 losses. Consequently, the loss for the outer training stage simplifies to:

$$\mathcal{L}_{C2}(\theta, \psi) = \mathcal{L}_{\text{MSE}}(\mathbf{x}, \hat{\mathbf{x}}). \quad (15)$$

The training procedure of cGAN-JSCC is summarized in Algorithm 2, which uses a two-stage training strategy. In the outer training stage, the encoder and the adversarially trained decoder are end-to-end trained using the MSE loss function to ensure high reconstruction performance. In the inner training stage, the U-Net-based generator and the patch-based discriminator in the decoder are trained adversarially by minimizing a joint loss that combines the adversarial loss and the L1 loss. This two-stage training strategy enables the system to achieve high reconstruction accuracy via optimization in the outer stage and enhances robustness to channel variations through adversarial training in the inner stage.

Fig. 4 illustrates the two-stage training architecture of cGAN-JSCC. The green area denotes the outer training stage that performs end-to-end training of the entire JSCC model, while the yellow area corresponds to the inner training stage

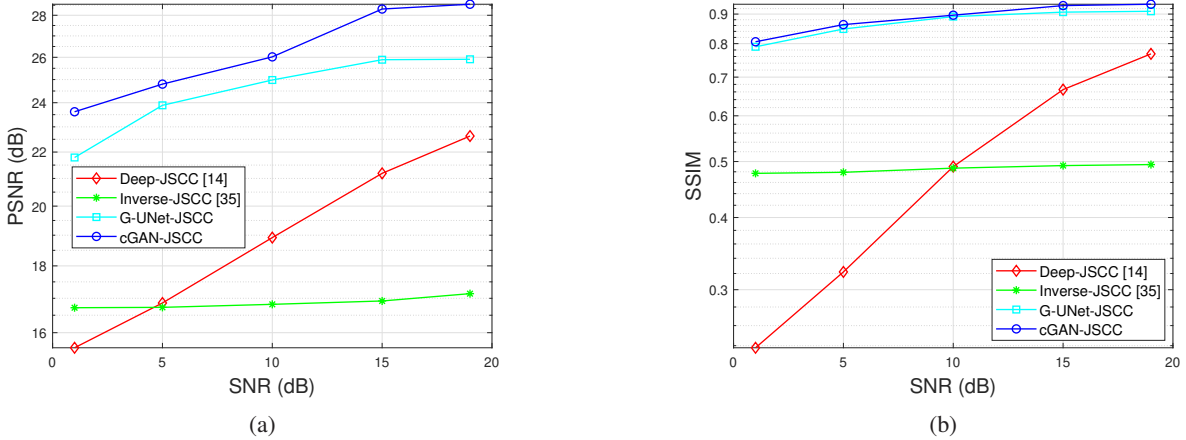


Fig. 5. Performance comparison of different JSCC reconstruction methods on the CIFAR-10 dataset at a compression ratio of  $r = 1/12$ : (a) PSNR and (b) SSIM versus channel SNR.

performing adversarial training. Specifically, in the outer stage, the encoder and the adversarially trained decoder are trained end-to-end using an MSE loss function. In the inner stage, embedded within the decoder's forward pass, the generator and the discriminator are adversarially trained to minimize the joint loss combining the adversarial and L1 losses. Similar to G-UNet-JSCC, cGAN-JSCC is also particularly suitable for practical deployment scenarios with resource-constrained encoders. It efficiently pairs a computationally-limited encoder with a powerful decoder, thereby achieving high reconstruction quality while maintaining relatively low computational overhead at the transmitter. During training, cGAN-JSCC undergoes both the outer and inner training stages. However, during the deployment (or inference) phase, only the encoder and the U-Net-based generator are used; the discriminator and the adversarial training process are no longer required.

#### IV. NUMERICAL RESULTS

This section presents the experimental results comparing the performance of the proposed G-UNet-JSCC and cGAN-JSCC methods. Both DeepJSCC methods were trained and tested over an AWGN channel, as defined in Eq. (3). We conducted experiments on low-resolution images from the CIFAR-10 dataset [44], using 50000 images for training and 10000 images for testing. All images in this dataset have a fixed size of  $32 \times 32 \times 3$ . For mid-resolution and high-resolution images, we used the CelebA dataset [45] and the CelebA-HQ dataset [40], respectively. The face images from the CelebA dataset were cropped to  $64 \times 64 \times 3$  patches, while those from the CelebA-HQ dataset were cropped to produce patches of dimensions  $256 \times 256 \times 3$ . The CelebA dataset contains 160000 training images and 10000 test images, while the CelebA-HQ dataset comprises 24000 images for training and 2000 images for testing. To mitigate memory constraints, the batch size was set to  $B = 1$  for training both cGAN-JSCC and G-UNet-JSCC on the aforementioned datasets. The models were trained for 20 epochs ( $E = 20$ ) under this configuration. All encoder and decoder networks were optimized using the Adam optimizer

with an initial learning rate of  $\eta = 0.001$ . We implemented the G-UNet-JSCC and cGAN-JSCC methods in Python 3.8.20 with TensorFlow 2.6.0. All experiments were performed on a workstation with an Intel Xeon Gold 6348 CPU, 383 GB of RAM, and an NVIDIA RTX A6000 GPU. For the G-UNet-JSCC scheme, we empirically set the hyperparameters  $\lambda_M$  and  $\lambda_S$  in Eq. (7) to 0.9 and 0.1, respectively.

To ensure that the target BCR  $r$  matches the actual BCR, the parameters  $k$  and  $c$  are determined as follows for all networks during both training and inference. Let  $n = H_I \times W_I \times C_I$ , where  $H_I$ ,  $W_I$ , and  $C_I$  represent the height, width, and number of channels of the source image, respectively. Then, we set  $k = \lfloor r \times n \rfloor$  and  $c = \lfloor k / (H_O \times W_O / 2) \rfloor$ , where  $\lfloor \cdot \rfloor$  denotes the floor function. Here,  $H_O$  and  $W_O$  denote the height and width of the feature map output by the last convolutional layer of the encoder, respectively.

##### A. Evaluation Metrics

To comprehensively evaluate the quality of JSCC reconstructions, we employ several performance metrics: PSNR for pixel-level fidelity, SSIM for structural similarity, and LPIPS for perceptual quality.

The PSNR is given by

$$\text{PSNR}(\mathbf{x}, \hat{\mathbf{x}}) = 10 \log_{10} \left( \frac{P_{\text{MAX}}^2}{\text{MSE}(\mathbf{x}, \hat{\mathbf{x}})} \right), \quad (16)$$

where  $P_{\text{MAX}} = 255$  denotes the maximum pixel value, and  $\text{MSE}(\mathbf{x}, \hat{\mathbf{x}})$  is the MSE between the original image  $\mathbf{x}$  and its reconstruction  $\hat{\mathbf{x}}$ .

The SSIM between images  $\mathbf{x}$  and  $\hat{\mathbf{x}}$  is defined as

$$\text{SSIM}(\mathbf{x}, \hat{\mathbf{x}}) = [l_u(\mathbf{x}, \hat{\mathbf{x}})]^\alpha [c(\mathbf{x}, \hat{\mathbf{x}})]^\beta [s(\mathbf{x}, \hat{\mathbf{x}})]^\gamma, \quad (17)$$

where  $l_u(\cdot)$ ,  $c(\cdot)$ , and  $s(\cdot)$  measure the luminance, contrast,

and structure similarity, respectively:

$$l_u(\mathbf{x}, \hat{\mathbf{x}}) = \frac{2\mu_{\mathbf{x}}\mu_{\hat{\mathbf{x}}} + C_1}{\mu_{\mathbf{x}}^2 + \mu_{\hat{\mathbf{x}}}^2 + C_1}, \quad (18)$$

$$c(\mathbf{x}, \hat{\mathbf{x}}) = \frac{2\sigma_{\mathbf{x}}\sigma_{\hat{\mathbf{x}}} + C_2}{\sigma_{\mathbf{x}}^2 + \sigma_{\hat{\mathbf{x}}}^2 + C_2}, \quad (19)$$

$$s(\mathbf{x}, \hat{\mathbf{x}}) = \frac{\sigma_{\mathbf{x}\hat{\mathbf{x}}} + C_3}{\sigma_{\mathbf{x}}\sigma_{\hat{\mathbf{x}}} + C_3}. \quad (20)$$

Here,  $\sigma_{\mathbf{x}\hat{\mathbf{x}}}$  denotes the sample covariance between  $\mathbf{x}$  and  $\hat{\mathbf{x}}$ . The standard deviation and the mean of  $\mathbf{x}$  are denoted by  $\sigma_{\mathbf{x}}$  and  $\mu_{\mathbf{x}}$ , respectively. Similarly,  $\sigma_{\hat{\mathbf{x}}}$  and  $\mu_{\hat{\mathbf{x}}}$  denote the standard deviation and the mean of  $\hat{\mathbf{x}}$ , respectively. The constants  $C_1$ ,  $C_2$ , and  $C_3$  are included for numerical stability. All parameters ( $\alpha, \beta, \gamma, C_1, C_2, C_3$ ) are set to their default values following the original implementation in [46].

The LPIPS metric was proposed in [33] to measure the perceptual quality between a source image and its reconstruction. This metric demonstrates superior alignment with human perception compared to conventional metrics like PSNR and SSIM. The metric works by computing the similarity between the feature activations of two image patches extracted from a pre-trained deep network (e.g., VGG or AlexNet). In this work, we employ the pre-trained VGG network. Lower LPIPS values indicate greater perceptual similarity between the images.

### B. Performance Evaluation of Proposed DeepJSCC Methods

This subsection compares four DeepJSCC methods: the proposed G-UNet-JSCC and cGAN-JSCC, Deep-JSCC [14], and Inverse-JSCC [35]. The evaluation is conducted on three image datasets of varying sizes: CIFAR-10, CelebA, and CelebA-HQ. To comprehensively evaluate the reconstruction quality, we employ three performance metrics: PSNR, SSIM, and LPIPS. In this work, we use the term Inverse-JSCC to denote the Inverse-JSCC framework from [35] without its pre-trained generator. Our implementation of the Inverse-JSCC model, which corresponds to the forward operator  $A$  in [35], is trained end-to-end using the MSE loss. Furthermore, we made several modifications to the original Inverse-JSCC architecture. First, the number of filters in all convolutional layers was reduced from 512 to 256. Second, to ensure compatibility, we inserted a convolutional layer before the decoder’s first attention module. This aligns the channel dimension of the reshaped encoder output with that of the first attention module in the Inverse-JSCC decoder. Finally, an additional convolutional layer was appended after the last attention feature (AF) module to reduce the number of output channels to three for RGB reconstruction.

Fig. 5 compares the PSNR and SSIM performance of various DeepJSCC methods over a range of channel SNRs. As shown in Fig. 5(a), cGAN-JSCC outperforms G-UNet-JSCC across all considered SNR regimes. This result indicates that adversarial training enables cGAN-JSCC to extract features more effectively than G-UNet-JSCC on low-resolution CIFAR-10 images. In addition, G-UNet-JSCC significantly surpasses Deep-JSCC, confirming its superiority over Deep-JSCC. Although Inverse-JSCC achieves higher PSNR than Deep-JSCC at low SNRs ( $\text{SNR} \leq 4$  dB), its performance

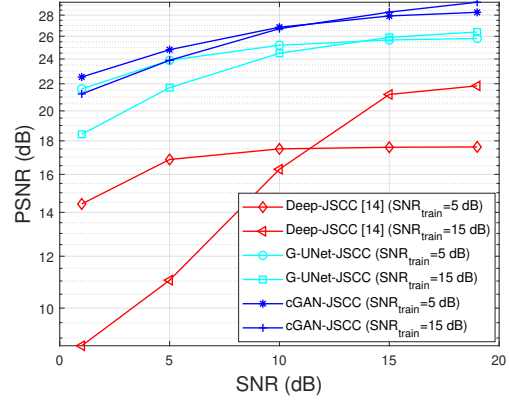


Fig. 6. Robustness of G-UNet-JSCC and cGAN-JSCC to SNR mismatch on the CIFAR-10 dataset at  $r = 1/12$ . Each model is trained at a specific SNR and tested across a wide range of SNRs.

exhibits limited improvement as the SNR increases. This is primarily because the aggressive downsampling used in the Inverse-JSCC encoder produces feature maps with insufficient information content for low-resolution images, thereby limiting the decoder’s reconstruction quality. Fig. 5(b) shows that cGAN-JSCC has the best SSIM performance among all the methods. G-UNet-JSCC significantly outperforms Inverse-JSCC. Moreover, G-UNet-JSCC achieves SSIM performance comparable to that of cGAN-JSCC, since it is trained by minimizing a weighted sum of MSE and SSIM losses. While Inverse-JSCC consistently surpasses Deep-JSCC at SNRs  $\leq 9$  dB, it shows only marginal SSIM improvement with increasing SNR. Overall, cGAN-JSCC outperforms G-UNet-JSCC in handling low-resolution CIFAR-10 images. Both cGAN-JSCC and G-UNet-JSCC achieve satisfactory PSNR and SSIM performance even at low SNRs. In contrast, Inverse-JSCC exhibits limited performance on such low-resolution images.

Next, we test the robustness of cGAN-JSCC and G-UNet-JSCC to channel SNR variations in Fig. 6. Each curve is obtained by training an end-to-end model at a fixed channel SNR, denoted as  $\text{SNR}_{\text{train}}$ , and then evaluating the reconstruction performance of the trained model on the CIFAR-10 test set under different test SNRs. Unlike conventional separation-based systems, the Deep-JSCC method proposed in [14] does not suffer from the severe “cliff effect” when the test SNR falls below  $\text{SNR}_{\text{train}}$ . Nevertheless, when  $\text{SNR}_{\text{train}} = 15$  dB, Deep-JSCC still exhibits significant performance degradation as the test SNR decreases from 15 dB to 1 dB. On the contrary, both cGAN-JSCC and G-UNet-JSCC show only a gradual degradation under the same conditions, demonstrating their superior robustness to channel SNR variations. Furthermore, cGAN-JSCC exhibits an even smaller performance drop than G-UNet-JSCC, confirming that cGAN-JSCC achieves the greatest robustness among all methods.

We present a visual comparison of different DeepJSCC methods on the CIFAR-10 dataset in Fig. 7. Although the reconstructions from both Inverse-JSCC and Deep-JSCC are blurry, Deep-JSCC preserves the image color and details more



Fig. 7. Visual comparison of JSCC reconstruction methods on the CIFAR-10 dataset at SNR = 10 dB and  $r = 1/12$ . The first row shows the original images, while the second to fifth rows present the reconstructions obtained by Deep-JSCC, Inverse-JSCC, G-UNet-JSCC, and cGAN-JSCC, respectively.

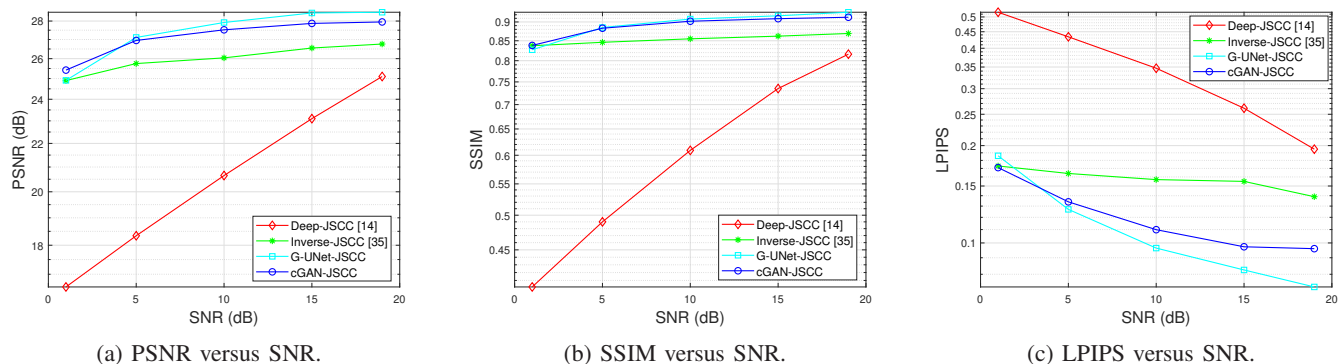


Fig. 8. Performance comparison of different JSCC reconstruction methods on the CelebA dataset at  $r = 1/12$ : (a) PSNR, (b) SSIM, and (c) LPIPS versus channel SNR.

effectively than Inverse-JSCC. In contrast, both cGAN-JSCC and G-UNet-JSCC produce reconstructions with significantly higher perceptual quality than those from Deep-JSCC. Moreover, cGAN-JSCC appears to capture the color and details of low-resolution CIFAR-10 images slightly better than G-UNet-JSCC.

Fig. 8 compares different DeepJSCC methods in terms of PSNR, SSIM, and LPIPS on the CelebA dataset across a range of channel SNR values. Inverse-JSCC significantly outperforms Deep-JSCC over all considered SNR regimes, maintaining satisfactory performance even under low SNR conditions. This result demonstrates that Inverse-JSCC maintains robust performance when processing mid-resolution CelebA images. Nevertheless, cGAN-JSCC outperforms Inverse-JSCC in terms of PSNR, SSIM, and LPIPS. Moreover, likely due to its adversarial training strategy, cGAN-JSCC surpasses G-UNet-JSCC at SNRs  $\leq 4$  dB, whereas G-UNet-JSCC outperforms cGAN-JSCC at SNRs  $\geq 4$  dB. Additionally, at SNRs  $\geq 4$

dB, the LPIPS performance gap between G-UNet-JSCC and cGAN-JSCC becomes larger as the SNR increases. Overall, both cGAN-JSCC and G-UNet-JSCC perform well on mid-resolution CelebA images.

Fig. 9 provides a visual comparison of different DeepJSCC methods on the CelebA dataset. The images reconstructed by Deep-JSCC are blurry, while those by Inverse-JSCC are of high perceptual quality. This indicates that Inverse-JSCC exhibits good performance on mid-resolution CelebA images. Both cGAN-JSCC and G-UNet-JSCC also generate reconstructions of high perceptual quality, with no visually significant difference between them. Moreover, the reconstructions of cGAN-JSCC and G-UNet-JSCC seem to preserve the color and fine details slightly better than those of Inverse-JSCC.

Fig. 10 compares the PSNR, SSIM, and LPIPS performance of various DeepJSCC methods on the CelebA-HQ dataset across varying channel SNRs. We observe that Inverse-JSCC outperforms Deep-JSCC in both pixel-wise fidelity and per-



Fig. 9. Visual comparison of JSCC reconstruction methods on the CelebA dataset at SNR = 10 dB and  $r = 1/12$ . The first row shows the original images. Reconstructions by Deep-JSCC, Inverse-JSCC, G-UNet-JSCC, and cGAN-JSCC are shown in rows 2 to 5, respectively.

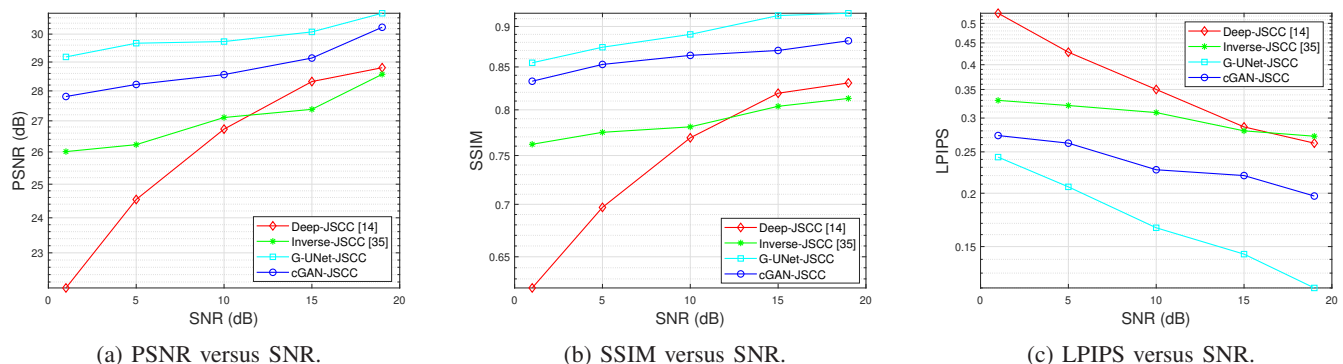


Fig. 10. Performance comparison of different reconstruction methods on the CelebA-HQ dataset at  $r = 1/12$ : (a) PSNR, (b) SSIM, and (c) LPIPS versus channel SNR.

ceptual quality at SNRs  $\leq 11$  dB, especially under low SNR conditions. This result demonstrates that Inverse-JSCC maintains good performance in low SNR regimes, which is consistent with [35]. cGAN-JSCC achieves better performance than Inverse-JSCC, whereas G-UNet-JSCC outperforms cGAN-JSCC in both pixel-level fidelity and perceptual quality across all considered SNR regimes. This indicates that G-UNet-JSCC performs better than cGAN-JSCC when dealing with high-resolution CelebA-HQ images.

Fig. 11 presents the visual comparison of different Deep-JSCC methods on the CelebA-HQ dataset at an SNR of 5 dB. Although Deep-JSCC reconstructs face images that are not blurry at SNR = 5 dB, it still fails to accurately reproduce the color and fine details of the original high-resolution images. In contrast, Inverse-JSCC produces reconstructions of high perceptual quality, thereby demonstrating its effectiveness on high-resolution CelebA-HQ images. However, it incurs

the highest computational complexity among all compared methods. Meanwhile, cGAN-JSCC and G-UNet-JSCC not only generate reconstructions of high perceptual quality but also appear to capture fine image details better than Inverse-JSCC. Notably, a semi-transparent artifact may appear on the high-resolution face images reconstructed by cGAN-JSCC, due to the instability of the adversarial training in cGAN-JSCC. Consequently, G-UNet-JSCC outperforms cGAN-JSCC on high-resolution CelebA-HQ images.

### C. Complexity Analysis

This subsection analyzes the computational complexity of the proposed G-UNet-JSCC and cGAN-JSCC methods, as well as other DeepJSCC approaches, such as Deep-JSCC and Inverse-JSCC. We adopt the number of floating-point operations (FLOPs) as the metric for computational complexity. For all DeepJSCC methods, the computational complexity is

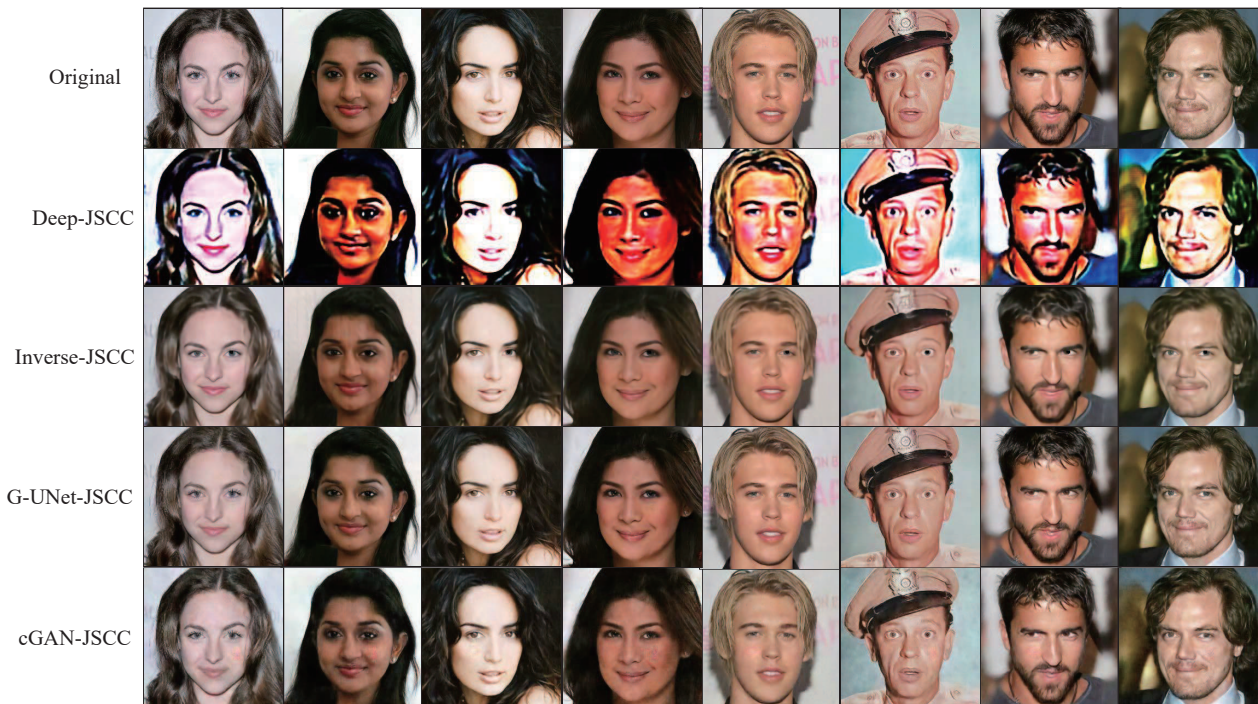


Fig. 11. Visual comparison of JSCC reconstruction methods on the Celeb-HQ dataset at SNR = 5 dB and  $r = 1/12$ . The first row shows the original images, while the second to fifth rows present the reconstructions obtained by Deep-JSCC, Inverse-JSCC, G-UNet-JSCC, and cGAN-JSCC, respectively.

mainly determined by their encoder and decoder networks. This is because these networks are primarily composed of 2D convolutional and transposed convolutional layers, which dominate the overall computational cost.

Following the analysis in [38], [47], the computational cost in FLOPs for the encoder of G-UNet-JSCC is expressed as

$$C_{E-G-UNet} \sim \mathcal{O} \left( \sum_{l=1}^L M_{l,h} M_{l,w} F_l^2 K_l K_{l-1} \right), \quad (21)$$

where  $L$  is the number of layers,  $F_l$  is the kernel size at the  $l$ -th layer,  $K_l$  and  $K_{l-1}$  denote the numbers of output and input feature maps for the  $l$ -th layer, respectively, and  $M_{l,h} \times M_{l,w}$  represents the size of the output feature map of the  $l$ -th layer. The FLOPs of the G-UNet-JSCC decoder are similarly given by  $C_{D-G-UNet} \sim \mathcal{O} \left( \sum_{l=1}^L M_{l,h} M_{l,w} F_l^2 K_l K_{l-1} \right)$ . Thus, the total FLOPs required for G-UNet-JSCC are given by summing those of its encoder and decoder:  $C_{G-UNet} = C_{E-G-UNet} + C_{D-G-UNet}$ . The total FLOPs required for other DeepJSCC methods (e.g., cGAN-JSCC, Deep-JSCC, and Inverse-JSCC) can be similarly obtained.

G-UNet-JSCC exhibits higher computational complexity than Deep-JSCC, primarily due to its more complex decoder architecture. cGAN-JSCC is slightly more complex than G-UNet-JSCC, since its decoder incorporates not only a U-Net-based generator but also an additional discriminator. Inverse-JSCC incurs the greatest computational cost in FLOPs among these methods. This results from its sophisticated architecture. Compared to cGAN-JSCC, Inverse-JSCC includes a larger number of feature maps, a deeper network structure, and more

complex modules such as attention mechanisms and residual blocks. Note that the number of input feature maps  $K_{l-1}$  for the transposed convolutional layers that incorporate skip connections is doubled, which further increases the FLOPs of the decoder due to channel concatenation.

## V. CONCLUSION

In this work, we proposed G-UNet-JSCC and cGAN-JSCC, two DeepJSCC methods based on deep generative architectures for wireless image transmission. G-UNet-JSCC comprises an encoder and a U-Net-based generator serving as the decoder. This architecture enables multi-scale feature fusion by combining low-level features with high-level features, thereby improving both pixel-level fidelity and perceptual quality. To further improve pixel-level fidelity, the encoder and the decoder are jointly optimized using a weighted sum of MSE and SSIM losses. Building upon G-UNet-JSCC, we further developed cGAN-JSCC by enhancing its decoder while retaining the same encoder. The decoder's generator is adversarially trained against a patch-based discriminator. cGAN-JSCC uses a two-stage training procedure. The outer stage trains the encoder and the decoder end-to-end using an MSE loss, while the inner stage adversarially trains the generator and the discriminator within the decoder by minimizing a joint adversarial and L1 loss. Extensive numerical experiments demonstrate that the proposed methods achieve high pixel-wise fidelity and perceptual quality on both high- and low-resolution images. For low-resolution images, cGAN-JSCC further achieves superior reconstruction performance

and greater robustness to channel SNR variations compared to G-UNet-JSCC.

## REFERENCES

- [1] C. E. Shannon, "A mathematical theory of communication," *Bell Syst. Tech. J.*, vol. 27, no. 3, pp. 379-423, Oct. 1948.
- [2] V. Kostina and S. Verdú, "Lossy joint source-channel coding in the finite blocklength regime," *IEEE Trans. Inf. Theory*, vol. 59, no. 5, pp. 2545-2575, May 2013.
- [3] S. T. Jose and A. A. Kulkarni, "Linear programming-based converses for finite blocklength lossy joint source-channel coding," *IEEE Trans. Inf. Theory*, vol. 63, no. 11, pp. 7066-7094, Nov. 2017.
- [4] A. Azari, M. Ozger and C. Cavdar, "Risk-aware resource allocation for URLLC: Challenges and strategies with machine learning," *IEEE Commun. Mag.*, vol. 57, no. 3, pp. 42-48, Mar. 2019.
- [5] M. Vaezi and F. Labeau, "Distributed source-channel coding based on real-field BCH codes," *IEEE Trans. Signal Process.*, vol. 62, no. 5, pp. 1171-1184, Mar. 2014.
- [6] F. Hekland, P. A. Floor, and T. A. Ramstad, "Shannon-kotel-nikov mappings in joint source-channel coding," *IEEE Trans. Commun.*, vol. 57, no. 1, pp. 94-105, Jan. 2009.
- [7] A. Golmohammadi and D. G. M. Mitchell, "Concatenated spatially coupled LDPC codes with sliding window decoding for joint source-channel coding," *IEEE Trans. Commun.*, vol. 70, no. 2, pp. 851-864, Feb. 2022.
- [8] L. Pu, Z. Wu, A. Bilgin, M. W. Marcellin, and B. Vasic, "LDPC-based iterative joint source-channel decoding for JPEG2000," *IEEE Trans. Image Process.*, vol. 16, no. 2, pp. 577-581, Feb. 2007.
- [9] Z. Peng, Y. -F. Huang, and D. J. Costello, "Turbo codes for image transmission-A joint channel and source decoding approach," *IEEE J. Sel. Areas in Commun.*, vol. 18, no. 6, pp. 868-879, Jun. 2000.
- [10] Z. Xuan and K. Narayanan, "Low-delay analog joint source-channel coding with deep learning," *IEEE Trans. Commun.*, vol. 71, no. 1, pp. 40-51, Jan. 2023.
- [11] D. B. Kurka and D. Gündüz, "DeepJSCC-f: Deep joint source-channel coding of images with feedback," *IEEE J. Sel. Areas Inf. Theory*, vol. 1, no. 1, pp. 178-193, May 2020.
- [12] T. -Y. Tung, D. B. Kurka, M. Jankowski, and D. Gündüz, "DeepJSCC-Q: Constellation constrained deep joint source-channel coding," *IEEE J. Sel. Areas Inf. Theory*, vol. 3, no. 4, pp. 720-731, Dec. 2022.
- [13] J. Xu, B. Ai, W. Chen, A. Yang, P. Sun, and M. Rodrigues, "Wireless image transmission using deep source channel coding with attention modules," *IEEE Trans. Circuits Syst. Video Technol.*, vol. 32, no. 4, pp. 2315-2328, Apr. 2022.
- [14] E. Boursoulatzé, D. B. Kurka, and D. Gündüz, "Deep joint source-channel coding for wireless image transmission," *IEEE Trans. Cogn. Commun. Netw.*, vol. 5, no. 3, pp. 567-579, Sep. 2019.
- [15] H. Wu, Y. Shao, K. Mikolajczyk, and D. Gündüz, "Channel-adaptive wireless image transmission with OFDM," *IEEE Wireless Commun. Lett.*, vol. 11, no. 11, pp. 2400-2404, Nov. 2022.
- [16] D. B. Kurka and D. Gündüz, "Bandwidth-agile image transmission with deep joint source-channel coding," *IEEE Trans. Wireless Commun.*, vol. 20, no. 12, pp. 8081-8095, Dec. 2021.
- [17] J. Xu, B. Ai, W. Chen, A. Yang, P. Sun, and M. Rodrigues, "Wireless image transmission using deep source channel coding with attention modules," *IEEE Trans. Circuits Syst. Video Technol.*, vol. 32, no. 4, pp. 2315-2328, Apr. 2022.
- [18] M. Yang and H. -S. Kim, "Deep joint source-channel coding for wireless image transmission with adaptive rate control," in *Proc. IEEE Int. Conf. Acoust., Speech Signal Process. (ICASSP)*, May 2022, 5193-5197.
- [19] W. Zhang, H. Zhang, H. Ma, H. Shao, N. Wang, and V. C. M. Leung, "Predictive and adaptive deep coding for wireless image transmission in semantic communication," *IEEE Trans. Wireless Commun.*, vol. 22, no. 8, pp. 5486-5501, Aug. 2023.
- [20] H. Wu, Y. Shao, C. Bian, K. Mikolajczyk, and D. Gündüz, "Deep joint source-channel coding for adaptive image transmission over MIMO channels," *IEEE Trans. Wireless Commun.*, vol. 23, no. 10, pp. 15002-15017, Oct. 2024.
- [21] H. Wu, Y. Shao, C. Bian, K. Mikolajczyk, and D. Gündüz, "Vision transformer for adaptive image transmission over MIMO channels," in *Proc. IEEE Int. Conf. Commun.*, May 2023, pp. 3702-3707.
- [22] T. -Y. Tung and D. Gündüz, "Deep joint source-channel and encryption coding: Secure semantic communications," in *Proc. IEEE Int. Conf. Commun. (ICC)*, May 2023, pp. 5620-5625.
- [23] J. Shi, Q. Zhang, W. Zeng, S. Li, and Z. Qin, "Secure transmission in wireless semantic communications with adversarial training," *IEEE Commun. Lett.*, vol. 29, no. 3, pp. 487-491, Mar. 2025.
- [24] X. Luo, Z. Chen, M. Tao, and F. Yang, "Encrypted semantic communication using adversarial training for privacy preserving," *IEEE Commun. Lett.*, vol. 27, no. 6, pp. 1486-1490, Jun. 2023.
- [25] H. Tang, H. Liu, and N. Sebe, "Unified generative adversarial networks for controllable image-to-image translation," *IEEE Trans. Image Process.*, vol. 29, pp. 8916-8929, 2020.
- [26] J. Zhu, T. Park, P. Isola, and A. A. Efros, "Unpaired image-to-image translation using cycle-consistent adversarial networks," in *Proc. IEEE Int. Conf. Comput. Vis.*, Venice, Italy, Oct. 2017, pp. 2242-2251.
- [27] P. Isola, J. Zhu, T. Zhou, and A. A. Efros, "Image-to-image translation with conditional adversarial networks," in *Proc. IEEE Conf. Comput. Vis. Pattern Recognit. (CVPR)*, Honolulu, HI, USA, Jul. 2017, pp. 5967-5976.
- [28] T. Wu et al., "CDDM: Channel denoising diffusion models for wireless semantic communications," *IEEE Trans. Wireless Commun.*, vol. 23, no. 9, pp. 11168-11183, Sep. 2024.
- [29] Y. Malur Saidutta, A. Abdi, and F. Fekri, "VAE for joint source-channel coding of distributed Gaussian sources over AWGN MAC," in *Proc. IEEE 21st Int. Workshop Signal Process. Adv. Wireless Commun. (SPAWC)*, May 2020, pp. 1-5.
- [30] Y. M. Saidutta, A. Abdi, and F. Fekri, "Joint source-channel coding over additive noise analog channels using mixture of variational autoencoders," *IEEE J. Sel. Areas Commun.*, vol. 39, no. 7, pp. 2000-2013, Jul. 2021.
- [31] T. Marchioro, N. Laurenti, and D. Gündüz, "Adversarial networks for secure wireless communications," in *Proc. IEEE Int. Conf. Acoust., Speech Signal Process. (ICASSP)*, May, 2020, pp. 8748-8752.
- [32] M. Yang, C. Bian, and H. Kim, "OFDM-guided deep joint source channel coding for wireless multipath fading channels," *IEEE Trans. Cogn. Commun. Netw.*, vol. 8, no. 2, pp. 584-599, Jun. 2022.
- [33] R. Zhang, P. Isola, A. A. Efros, E. Shechtman, and O. Wang, "The unreasonable effectiveness of deep features as a perceptual metric," in *Proc. IEEE/CVF Conf. Comput. Vis. Pattern Recognit.*, Jun. 2018, pp. 586-595.
- [34] T. Karras, S. Laine, M. Aittala, J. Hellsten, J. Lehtinen, and T. Aila, "Analyzing and improving the image quality of StyleGAN," in *Proc. CVPR*, Jun. 2020, pp. 8110-8119.
- [35] E. Erdemir, T. -Y. Tung, P. L. Dragotti, and D. Gündüz, "Generative joint source-channel coding for semantic image transmission," *IEEE J. Sel. Areas Commun.*, vol. 41, no. 8, pp. 2645-2657, Aug. 2023.
- [36] M. Ye, X. Liang, C. Pan, Y. Xu, M. Jiang, and C. Li, "GAN-based near-field channel estimation for extremely large-scale MIMO systems," *IEEE Trans. Green Commun. Netw.*, vol. 9, no. 1, pp. 304-316, Mar. 2025.
- [37] M. Ye, C. Pan, Y. Xu, and C. Li, "Generative adversarial networks-based channel estimation for intelligent reflecting surface assisted mmWave MIMO systems," *IEEE Trans. Cogn. Commun. Netw.*, vol. 10, no. 5, pp. 1883-1896, Oct. 2024.
- [38] M. Ye et al., "Improved conditional GAN-based channel estimation for MIMO-OFDM systems," *IEEE Trans. Cogn. Commun. Netw.*, vol. 12, pp. 2085-2099, 2026.
- [39] O. Ronneberger, P. Fischer, and T. Brox, "U-net: Convolutional networks for biomedical image segmentation," in *Proc. Inf. Conf. Medical Image Comput. Computing-Assisted Intervention (MICCAI)*, Nov. 2015, pp. 234-241.
- [40] T. Karras, T. Aila, S. Laine, and J. Lehtinen, "Progressive growing of GANs for improved quality, stability, and variation," 2017, *arXiv:1710.10196*.
- [41] Y. Dong, H. Wang, and Y. -D. Yao, "Channel estimation for one-bit multiuser massive MIMO using conditional GAN," *IEEE Commun. Lett.*, vol. 25, no. 3, pp. 854-858, Mar. 2021.
- [42] I. Goodfellow et al., "Generative adversarial nets," in *Advances in Neural Information Processing Systems*, vol. 27. Red Hook, NY, USA: Curran Assoc., 2014.
- [43] C. Ledig et al., "Photo-realistic single image super-resolution using a generative adversarial network," in *Proc. IEEE Conf. Comput. Vis. Pattern Recognit.*, 2017, pp. 4681-4690.
- [44] A. Krizhevsky, "Learning multiple layers of features from tiny images," Univ. Toronto, Toronto, ON, Canada, Rep. TR-2009, 2009.
- [45] Z. Liu, P. Luo, X. Wang, and X. Tang, "Deep learning face attributes in the wild," in *Proc. IEEE Int. Conf. Comput. Vis. (ICCV)*, Santiago, Chile, 2015, pp. 3730-3738.

- [46] Z. Wang, A. C. Bovik, H. R. Sheikh, and E. P. Simoncelli, "Image quality assessment: From error visibility to structural similarity," *IEEE Trans. Image Process.*, vol. 13, no. 4, pp. 600-612, Apr. 2004.
- [47] K. He and J. Sun, "Convolutional neural networks at constrained time cost," in *Proc. IEEE Conf. Comput. Vis. Pattern Recognit. (CVPR)*, Boston, MA, USA, Jun. 2015, pp. 5353-5360.